Failure Surfaces for Finitely Strained Two-Phase Periodic Solids Under General In-Plane Loading

N. Triantafyllidis[1]

M. D. Nestorović

Department of Aerospace Engineering,
The University of Michigan,
Ann Arbor, MI 48109-2140

M. W. Schraad
Theoretical Division,
Los Alamos National Laboratory,
Los Alamos, NM 87545

For ductile solids with periodic microstructures (e.g., honeycombs, fiber-reinforced composites, cellular solids) which are loaded primarily in compression, their ultimate failure is related to the onset of a buckling mode. Consequently, for periodic solids of infinite extent, one can define as the onset of failure the first occurrence of a bifurcation in the fundamental solution, for which all cells deform identically. By following all possible loading paths in strain or stress space, one can construct onset-of-failure surfaces for finitely strained, rate-independent solids with arbitrary microstructures. The calculations required are based on a Bloch wave analysis on the deformed unit cell. The presentation of the general theory is followed by the description of a numerical algorithm which reduces the size of stability matrices by an order of magnitude, thus improving the computational efficiency for the case of continuum unit cells. The theory is subsequently applied to porous and particle-reinforced hyperelastic solids with circular inclusions of variable stiffness. The corresponding failure surfaces in strain-space, the wavelength of the instabilities, and their dependence on micro-geometry and macroscopic loading conditions are presented and discussed. [DOI: 10.1115/1.2126695]

1 Introduction and Motivation

The issue of failure in composites is both a fundamental and also an extremely diverse one in solid mechanics. The fundamental aspect of the problem pertains to questions like what constitutes failure, when does failure start, and the possibility of predicting the onset-of-failure by investigating appropriately averaged (homogenized) material properties of the composite. The extreme diversity of the problem is due on one hand to the infinite variety of possible materials and microstructures and on the other hand to an equally large number of corresponding failure mechanisms.

In the interest of (relative) simplicity, attention is hereby focused in ductile, periodic (and nearly periodic) composites that are capable of sustaining large strains. These solids have a failure mechanism—usually a localized deformation mode—that is initiated by a buckling type instability. Moreover, the existence of a clearly identifiable unit cell allows modeling consistency and the possibility of controllable and repeatable experiments. There are many applications of engineering interest that fall into this category, such as fiber-reinforced composites, honeycomb, and cellular solids, just to name a few.

More specifically, of interest here is the relation between the onset of microscopic failure and the corresponding macroscopic properties of periodic, finitely strained ductile solids. The connection between the onset of microscopic buckling and the corresponding loss of ellipticity of the incremental moduli of the homogenized solid was first established by [1] for the special case of an incompressible, hyperelastic composite under plane strain conditions. Subsequent work by [2] proved the completeness of the Bloch wave representation for the bifurcation eigenmode in finitely strained, three-dimensional periodic solids with arbitrary unit cells. In the same paper it also was shown that if the wavelength of the bifurcation eigenmode is infinite (compared to the unit cell size), the corresponding instability of the periodic principal solution can be detected as a loss of ellipticity of the corresponding homogenized tangent moduli of the solid. Based on these general results, [3] defined the onset-of-failure surfaces in stress and strain space for periodic solids, a concept which was subsequently applied to truss-like structures by [4], to aluminum honeycomb by [5] and more recently to the case of fiber-reinforced composites under combined normal and shear strains by [6] and to three-dimensional Kelvin foams [7].

Due to the time-consuming nature of the Bloch wave stability calculations, only layered two-dimensional microstructures (for fiber reinforced composites under plane strain) and truss-like structures in two and three dimensions so far have been considered. The present paper, motivated by interest in the behavior of periodic porous and particle reinforced solids, is the first—to the best of the authors' knowledge—to deal with the microscopic and macroscopic stability of periodic continua having unit cells of commensurate dimensions in each direction, a task that requires the development of a novel, specialized numerical procedure.

The outline of the paper is a follows: The general mathematical theory, allowing for the construction of the onset-of-failure surfaces, is given in Sec. 2. The material description, macroscopic loading conditions, and the finite element method (f.e.m.)-based condensation algorithm that allows an efficient application of the Bloch wave analysis for the determination of the onset of microscopic instabilities are presented in Sec. 3. Section 4 presents the calculation results for the onset of microscopic and macroscopic failure of a compressible neo-Hookean, finitely strained periodic solid under various (orthotropic and non) plane strain conditions. The microgeometry considered is two phase with circular inclusions under two different arrangements: square and diagonal, both having the same volume fraction. The microscopic and macroscopic onset-of-failure surfaces for porous and rigid inclusion-reinforced solids are constructed by varying the inclusion-to-

[1]Corresponding author.

Contributed by the Applied Mechanics Division of ASME for publication in the JOURNAL OF APPLIED MECHANICS. Manuscript received February 9, 2005; final manuscript received September 1, 2005. Review conducted by R. M. McMeeking. Discussion on the paper should be addressed to the Editor, Prof. Robert M. McMeeking, Journal of Applied Mechanics, Department of Mechanical and Environmental Engineering, University of California—Santa Barbara, Santa Barbara, CA 93106-5070, and will be accepted until four months after final publication in the paper itself in the ASME JOURNAL OF APPLIED MECHANICS.

matrix stiffness ratio. Porous solids are found to be considerably more unstable than inclusion-reinforced solids under biaxial compression, but, in contrast to the latter, the failure of the porous solids is relatively insensitive to the microgeometry and involves critical modes with finite wavelengths. The presentation concludes with a discussion in Sec. 5.

2 Problem Formulation

In this section the "*onset-of-failure surface*" concept is formulated for an infinite, rate-independent solid with a perfectly periodic microstructure, which is subjected to an arbitrary, quasi-static macroscopic loading. As explained in the Introduction, the ultimate failure mechanism for a ductile solid with periodic microstructure often is related to the onset of a buckling-type instability. Consequently, the onset-of-failure surface is defined as the first occurrence of a bifurcation in the fundamental periodic solution, for which all cells deform identically. By using radial loading paths emerging from the stress-free state in macroscopic strain or stress space, one can construct onset-of-failure surfaces by connecting the failure points for all such paths.

The first part of this section presents the "*microscopic onset-of-failure surface*" concept, which is based on the investigation of all possible bounded modes of instability with wavelengths that are commensurate with the size of the unit cell, also termed "*local*" modes. Since the corresponding calculations are exceedingly time consuming (all wavelengths must be investigated along each coordinate direction), a "*macroscopic onset-of-failure surface*" concept is introduced in the second part, which is based on the investigation of instability modes with wavelengths that are much larger than the size of the unit cell, also termed "*global*" modes. Hence, by definition, the more accurate and also more computationally intensive microscopic onset-of-failure surface of a periodic solid always lies inside its macroscopic counterpart. The latter onset-of-failure surface only requires checking of rank one convexity of the solid's homogenized tangent moduli and is therefore considerably less time consuming to construct.

The problem is formulated in two dimensions, since all numerical calculations will be based on a two-dimensional application. However, a generalization to three dimensions is straightforward and is accomplished by enlarging the range of indices (from 1–2 to 1–3). Also notice that the onset-of-failure surface concept is valid for any rate-independent, i.e., elastic or elastoplastic, solid. However, the onset-of-failure surface is independent of the load path used in its determination only for elastic solids, because of the path-independent nature of their constitutive response. The application presented in the next section falls in this category since it pertains to a rubber-elastic material.

2.1 Microscopic Onset-of-Failure Surface. Consider a solid which occupies a domain V (with boundary ∂V) in its underformed (stress-free) state, which is used as the reference configuration. The solid has a regular, perfectly periodic microstructure with a fundamental building block D (with boundary ∂D), called the "*unit cell*," as shown in Fig. 1. The solid is deformed in the X_1-X_2 plane, under finite, plane strain conditions, and a full Lagrangian formulation of the problem is adopted. Material points in the solid are identified by their initial position vector $\mathbf{X}$, while the current position vector of the same point is denoted by $\mathbf{x}$. The displacement of each material point $\mathbf{X}$ is denoted by $\mathbf{u}$ where $\mathbf{u} \equiv \mathbf{x} - \mathbf{X}$. The deformation gradient at $\mathbf{X}$, a quantity that measures the deformation in the neighborhood of each point, is denoted by $\mathbf{F} \equiv \partial \mathbf{x} / \partial \mathbf{X}$.

The material in each phase of the unit cell follows a rate-independent, incrementally linear constitutive law that can be written in the following form[2]:

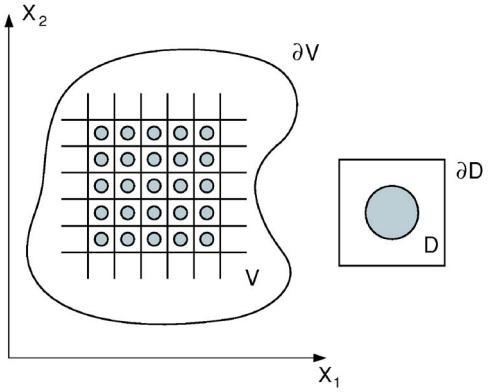

Fig. 1 Schematic representation of an infinite solid with a perfectly periodic microstructure and its corresponding unit cell. The solid is deformed under finite plane strain conditions in the X_1-X_2 plane.

$$\dot{\mathbf{\Pi}}_{ji}(\lambda, \mathbf{X}) = L_{ijkl}(\lambda, \mathbf{X}) \dot{F}_{kl}; \quad \dot{F}_{kl} = v_{k,l}, \tag{2.1}$$

in which $\dot{\mathbf{\Pi}}$ is the rate of the first Piola-Kirchhoff stress tensor and its work conjugate quantity $\dot{\mathbf{F}}$ is the rate of the deformation gradient, a function of the displacement rate $\mathbf{v}(\mathbf{X}) \equiv \dot{\mathbf{u}}$. For the quasi-static loading conditions considered here, by the rate of a field quantity one designates its derivative with respect to any time-like parameter which increases monotonically with the evolution of the loading process.

The incremental (tangent) moduli tensor $\mathbf{L}$ characterizes the material's instantaneous response in the neighborhood of $\mathbf{X}$ and is a function of the material properties and the current equilibrium state that can be described by a set of internal variables. Every loading process, assuming that it produces a unique response called the "*principal equilibrium path*," can be parametrized in terms of a scalar quantity λ, referred to as the "*load parameter*." Because the current state of the material, i.e., the stresses and internal variables in the neighborhood of $\mathbf{X}$, can be expressed in terms of the load parameter λ, the incremental moduli tensor $\mathbf{L}$ is fully characterized by λ as stated in (2.1). For the applications of interest here, it suffices to say that the incremental moduli tensor $\mathbf{L}$ possesses major symmetry, namely,

$$L_{ijkl}(\lambda, \mathbf{X}) = L_{klij}(\lambda, \mathbf{X}), \tag{2.2}$$

which is a condition satisfied by a wide range of rate-independent solids. The importance of this condition will be explained below. One must also mention here that $\mathbf{L}$ is a "*D-periodic*" function of $\mathbf{X}$, since the principal solution, whose stability is under investigation, has the translational symmetry of the microstructure (see Fig. 1)

$$\mathbf{L}(\lambda, X_1, X_2) = \mathbf{L}(\lambda, X_1 + n_1 L_1, X_1 + n_1 L_1), \tag{2.3}$$

with n_1, n_2 arbitrary integers. The translational symmetry condition is equivalent to ignoring boundary effects due to the application of surface loads and considering the stability of the interior region in periodic solids.

In this work, the stability of the principal equilibrium path is under investigation Hill [8] was the first to place the bifurcation and stability criteria for rate-independent, elastoplastic solids on a firm mathematical foundation. He presented the sufficient conditions for the exclusion of bifurcation in the incremental (rate one) problem of an elastoplastic solid and conjectured that these conditions also guarantee uniqueness. Moreover, he investigated the stability in elastoplastic problems by means of calculating the dissipation produced by small perturbations about the state in question, and further showed that his criterion for the exclusion of rate one bifurcation was sufficient for stability in the above-described

[2]Here and subsequently, Latin indexes range from 1 to 2, unless indicated differently. Einstein's summation convention is implied over repeated indexes.

sense. It was shown subsequently by [9] that Hill's stability criterion, based on the elastic moduli evaluated at the point of the loading path under investigation, implies the exclusion of bifurcation in any rate along the principal equilibrium path.

Thus, the stability of the rate-independent solid considered here is governed by Hill's stability criterion, which is based on the positive definiteness of a functional $\mathcal{F}_V$, defined on V, which is quadratic in the displacement rate field $\mathbf{v}(\mathbf{X})$. Therefore, a deformed state (characterized by λ) on the principal equilibrium path is stable if the minimum eigenvalue $\beta(\lambda)$ of the above-mentioned stability functional is positive,

$$\beta(\lambda) = \min_{\mathbf{v}}(\mathcal{F}_V(\lambda,\mathbf{v})/\|\mathbf{v}\|_V^2);$$

$$\mathcal{F}_V(\lambda,\mathbf{v}) \equiv \int_V \bar{v}_{i,j} L_{ijkl}(\lambda,\mathbf{X}) v_{k,l}\, dV, \tag{2.4}$$

$$\|\mathbf{v}\|_V^2 \equiv \int_V \bar{v}_{m,n} v_{m,n}\, dV,$$

when the minimum is taken over all kinematically admissible functions $\mathbf{v}$, i.e., all functions that are continuous in V and vanish on those points of the boundary ∂V where the displacement (essential) boundary conditions are prescribed. Furthermore, $\bar{\mathbf{v}}$ is the complex conjugate of the field $\mathbf{v}$. The assumed major symmetry of the incremental moduli $\mathbf{L}$ in (2.2) guarantees that all eigenvalues of the above-described quadratic functional are real.

The stability definition (2.4) pertains to a solid of finite size. A closer examination of (2.3) shows that solids of infinite extent can be included by considering locally integrable, bounded functions $\mathbf{v}$ and progressively increasing the size of the domain from a finite size V to R^2, while ensuring that the ratio defining the eigenvalue is finite. The corresponding Euler-Lagrange equation in R^2 is

$$(L_{ijkl}(\lambda,\mathbf{X}) v_{k,l} - \beta(\lambda) v_{i,j})_{,j} = 0. \tag{2.5}$$

For the perfectly periodic solids of infinite extent considered in this work, it has been shown by [2] that the eigenmodes $\mathbf{v}(\mathbf{X})$ of the problem (2.5) always can be expressed as[3]

$$\mathbf{v}(\mathbf{X}) = \mathbf{p}(\mathbf{X})\exp(i\boldsymbol{\omega}\cdot\mathbf{X}), \quad (\omega_1 L_1, \omega_2 L_2) \in \{(0,2\pi)\times(0,2\pi)\} \tag{2.6}$$

in which $\boldsymbol{\omega} \equiv (\omega_1, \omega_2)$ is the wave number of the eigenmode and $\mathbf{p}(\mathbf{X})$ is a D-periodic function, i.e., $\mathbf{p}$ satisfies (2.3) in which $\mathbf{L}$ is replaced by $\mathbf{p}$.

Consequently, to find the minimum eigenvalue β of $\mathcal{F}_V$, instead of scanning over all the bounded, locally integrable functions $\mathbf{v}$ on R^2, it suffices to scan over all D-periodic functions $\mathbf{p}$ and over all the wave numbers $\boldsymbol{\omega}$ in the appropriate domain of Fourier space,

$$\beta(\lambda) = \inf_{\boldsymbol{\omega}}[\gamma(\lambda,\boldsymbol{\omega})],$$
$$\gamma(\lambda,\boldsymbol{\omega}) \equiv \min_{\mathbf{p}}[\mathcal{F}_D(\lambda,\mathbf{p}\exp(i\boldsymbol{\omega}\cdot\mathbf{X}))/\|\mathbf{p}\exp(i\boldsymbol{\omega}\cdot\mathbf{X})\|_D^2], \tag{2.7}$$

with the D subscript in $\mathcal{F}$ and in $\|\mathbf{v}\|$ denoting that the corresponding quantities are defined by the same expressions as in (2.4) with the difference that the integration is now over the unit cell D instead of the entire domain V. Also note that the inf symbol has been used for the minimization with respect to $\boldsymbol{\omega}$ since $\gamma(\lambda,\boldsymbol{\omega})$ might have a singular point at $\boldsymbol{\omega}=\mathbf{0}$, as will be discussed subsequently in detail.

For any physically meaningful problem, the periodic solid under investigation is stable in its undeformed (stress-free) state, i.e., $\beta(0)>0$. As the load parameter λ increases monotonically from zero, $\beta(\lambda)$ decreases. The initially unique and stable principal, D-periodic, solution will at some load level cease to be unique, since nature always finds a way to go from a higher symmetry to a lower symmetry state. This first instability is detected by the lowest root of $\beta(\lambda)$, which is termed the "*microscopic critical load parameter*" and is denoted by λ_c,

$$\beta(\lambda_c) = 0, \quad \lambda_c = \inf_{\boldsymbol{\omega}}[\lambda_m(\boldsymbol{\omega})],$$
$$\gamma(\lambda_m(\boldsymbol{\omega}),\boldsymbol{\omega}) = 0, \quad \gamma(\lambda,\boldsymbol{\omega}) > 0, \quad \text{for } 0 \leqslant \lambda < \lambda_m. \tag{2.8}$$

In other words, $\lambda_m(\boldsymbol{\omega})$ is the lowest λ root of $\gamma(\lambda,\boldsymbol{\omega})$ for a fixed value of $\boldsymbol{\omega}$. The locus of all the macroscopic stresses or strains evaluated at λ_c for all loading paths constitutes the microscopic onset-of-failure surface in the corresponding macroscopic stress or strain space. Some important remarks about the nature of the eigenmode corresponding to λ_c are now in order.

From Eqs. (2.7) and (2.8) the determination of the load corresponding to the onset of a microscopic failure λ_c along a given load path consists of finding the lowest point of the surface $\lambda_m(\boldsymbol{\omega})$ in a λ_m versus ω_1,ω_2 graph. This surface need not be smooth. Quite frequently, numerical calculations of these surfaces show (see [5]) the presence of a singular point in the neighborhood of $\boldsymbol{\omega}=\mathbf{0}$. The physical reason for this singularity is due to the fact that in the neighborhood of $\boldsymbol{\omega}=\mathbf{0}$ one finds, by inspecting (2.6), two physically different types of modes: the strictly periodic modes $\boldsymbol{\omega}=\mathbf{0}$, $\mathbf{v}=\mathbf{p}$, and the long-wavelength modes $\boldsymbol{\omega}\to\mathbf{0}$, $\mathbf{v}\neq\mathbf{p}$, which have wavelengths much larger that the unit cell dimensions. This remark explains why the inf symbol is needed in the definition for the critical load in (2.7).

Thus, the following possibilities exist for the microscopic critical load, according to the wavelength of its corresponding mode. If $\lambda_c=\lambda_m(\boldsymbol{\omega}_c)$ where $\boldsymbol{\omega}_c\neq\mathbf{0}$ (mod 2π, assuming without loss of generality a square unit cell of unit side), the onset of microscopic failure corresponds to a truly local mode with a wavelength that is commensurate with the size of the unit cell. If $\lambda_c=\lambda_m(\boldsymbol{\omega}_c\to\mathbf{0})$ and $\boldsymbol{\omega}_c\to\mathbf{0}$ is a regular point of λ_m, the critical mode is still a local mode that is D periodic. If, however, at the limit $\boldsymbol{\omega}_c\to\mathbf{0}$ the surface λ_m is singular, then the corresponding eigenmode is global in nature, because its characteristic wavelength is much larger than the unit cell dimensions. The critical load in this case can be determined by a much simpler calculation, as will be discussed in the next subsection that deals with macroscopic onset-of-failure-type modes.

2.2 Macroscopic Onset-of-Failure Surface. As explained above, the determination of the microscopic onset-of-failure surface is a computationally intensive task. It is reasonable to question whether any relevant stability information can be obtained by considering the macroscopic (averaged) properties of the periodic solid. It turns out that for periodic solids there is a consistent and unambiguous definition of their macroscopic response in terms of the macroscopic, also termed "*homogenized*," tangent moduli of the solid that relates the average first Piola-Kirchhoff strain rate to the average rate of the deformation gradient

$$\langle \dot{\Pi}_{ji} \rangle = L^H_{ijkl}(\lambda)\langle \dot{F}_{kl}\rangle, \quad \langle f\rangle \equiv \frac{1}{\mathrm{vol}D}\int_D f\, dV. \tag{2.9}$$

For periodic solids, the homogenized incremental moduli tensor $\mathbf{L}^H$ is determined by

[3]The solutions to linear equations with periodic coefficients, in more than one dimension, are commonly named "*Bloch waves*" in physics literature.

$$\langle \dot{F}_{ij}\rangle L^H_{ijkl}(\lambda)\langle \dot{F}_{kl}\rangle = \min_{\mathbf{p}}\left(\frac{1}{\mathrm{vol}D}\int_D (\langle \dot{F}_{ij}\rangle + p_{i,j})L_{ijkl}(\lambda,\mathbf{X})(\langle \dot{F}_{kl}\rangle + p_{k,l})dV\right), \tag{2.10}$$

where $\langle \dot{\mathbf{F}}\rangle$ is an arbitrary rank two tensor and $\mathbf{p}$ any D-periodic function. From the above definition, a straightforward calculation procedure can be established from which, given the incremental moduli on each point $\mathbf{X}$ of the unit cell evaluated at the principal solution at load λ, one can determine the homogenized moduli tensor $\mathbf{L}^H(\lambda)$.

A macroscopic measure of the stability of the periodic solid at load λ can thus be defined, in an analogous way to the microscopic case in (2.4), by

$$B(\lambda) = \min_{\mathbf{a},\mathbf{n}} \Gamma(\lambda,\mathbf{a},\mathbf{n}),$$

$$\Gamma(\lambda,\mathbf{a},\mathbf{n}) \equiv a_i n_j L^H_{ijkl}(\lambda) a_k n_l \quad (\|\mathbf{a}\| = \|\mathbf{n}\| = 1),$$

in which the minimum is taken over all unit vectors $\mathbf{a}$ and $\mathbf{n}$. A positive $B(\lambda)$ guarantees the rank one convexity of the (2.11) material, thus excluding discontinuous solutions in boundary value problems formulated in terms of the macroscopic tangent moduli. Notice that the definition for $B(\lambda)$ in (2.11) does not involve arbitrary tensors, but only rank one tensors $\mathbf{an}$. There are several physical explanations for this fact, the most important one being that local convexity of the homogenized moduli with respect to tensors of arbitrary rank is too restrictive and physically unrealistic (it would imply uniqueness in corresponding boundary value problems, an unacceptable situation for nonlinear solids).

One can now proceed to define the "*macroscopic critical load parameter*," denoted by λ_h as the lowest root of $B(\lambda)$,

$$B(\lambda_h) = 0, \quad \lambda_h = \min_{\mathbf{a},\mathbf{n}}(\lambda_M(\mathbf{a},\mathbf{n})),$$
$$\Gamma(\lambda_M(\mathbf{a},\mathbf{n}),\mathbf{a},\mathbf{n}) = 0, \quad \Gamma(\lambda,\mathbf{a},\mathbf{n}) > 0, \quad \text{for } 0 \leqslant \lambda < \lambda_M. \tag{2.12}$$

In other words $\lambda_M(\mathbf{a},\mathbf{n})$ is the lowest λ root of $\Gamma(\lambda,\mathbf{a},\mathbf{n})$ for fixed $\mathbf{a}$, $\mathbf{n}$.

There is an intimate connection between the microscopic and macroscopic critical loads λ_c and λ_h,

$$\lambda_h = \inf_{\boldsymbol{\omega}\to 0} \lambda_m(\boldsymbol{\omega}), \tag{2.13}$$

assuming of course that $\mathbf{L}^H$ exists, which requires uniqueness in the solution of the unit cell boundary value problem, thus excluding a first bifurcation with $\boldsymbol{\omega}_c = \mathbf{0}$ (a periodic mode with a period equal to the unit cell size). In all the numerical calculations reported here, this is indeed the case, i.e., $\boldsymbol{\omega}_c \neq \mathbf{0}$. However, the periodic solids with a first buckling mode corresponding to $\boldsymbol{\omega}_c = \mathbf{0}$ are frequently encountered. For example, critical microbuckling modes with wavelengths equal to the dimensions of the unit cell are encountered in cellular solids, because of their very flexible unit cells (the interested reader is referred to [5]).

3 Solution Procedure

The general theory for the onset-of-failure in periodic solids of infinite extent, presented in Sec. 2, is applied to a class of finitely strained, two-phase hyperelastic solids, which are subjected to arbitrary loading under plane strain conditions. This section is divided into three parts, starting with the description of the microgeometry and the imposed macroscopic loading, continuing with the constitutive model and ending with the presentation of the f.e.m.-based numerical algorithm.

3.1 Geometry and Loading Conditions. Of interest here are two-phase periodic solids consisting of circular inclusions perfectly bonded to their surrounding matrix. By adjusting the ratio of the inclusion-to-matrix stiffnesses, one can cover the range from voided to rigid fiber-reinforced solids with the same microgeometry. Two different microstructure geometries are considered for these two-phase periodic solids: A square arrangement of circular inclusions shown in Fig. 2(*a*) and a diagonal arrangement of the same inclusions shown in Fig. 2(*b*). Both microstructures considered have the same volume fraction for the inclusions. Consequently, as seen in Fig. 2(*a*), the unit cell dimensions for the square microgeometry are $L_1 = L_2 = L$, while the unit cell dimensions for the diagonal microgeometry depicted in Fig. 2(*b*) are $L_1 = L$, $L_2 = 2L$. The radius of the inclusion R is the same for both microgeometries and hence the volume fraction of the inclusions is $(\pi/4)(R/L)^2$.

The macroscopic loading imposed on the infinite periodic solid is such that the corresponding average deformation has principal stretch ratios λ_1 and λ_2 at a fixed angle θ with respect to X_1, X_2 (the solid's axes of orthotropy in the reference configuration). By ignoring macroscopic rigid body rotations ($\langle \mathbf{R}\rangle = \mathbf{I}$), the macroscopic (average) deformation gradient $\langle \mathbf{F}\rangle$ coincides with the macroscopic right stretch tensor $\langle \mathbf{U}\rangle$ and left stretch tensor $\langle \mathbf{V}\rangle$ and can be expressed as

$$\langle F_{ij}\rangle = \langle U_{ij}\rangle = \langle V_{ij}\rangle = \begin{bmatrix} \cos\theta & -\sin\theta \\ \sin\theta & \cos\theta \end{bmatrix}\begin{bmatrix} \lambda_1 & 0 \\ 0 & \lambda_2 \end{bmatrix}\begin{bmatrix} \cos\theta & \sin\theta \\ -\sin\theta & \cos\theta \end{bmatrix}. \tag{3.1}$$

The current deformed state of the solid is achieved through a proportional straining path in principal strain space. More specifically, it is assumed that the ratio of the principal logarithmic strains ε_i is fixed,

$$\ln(\lambda_1) \equiv \varepsilon_1 = \lambda\cos\varphi, \quad \ln(\lambda_2) \equiv \varepsilon_2 = \lambda\sin\varphi. \tag{3.2}$$

in which λ is the monotonically increasing "*load parameter*" of the process and φ is the "*load path*" angle.

The macroscopic and microscopic onset-of-failure surfaces cal-

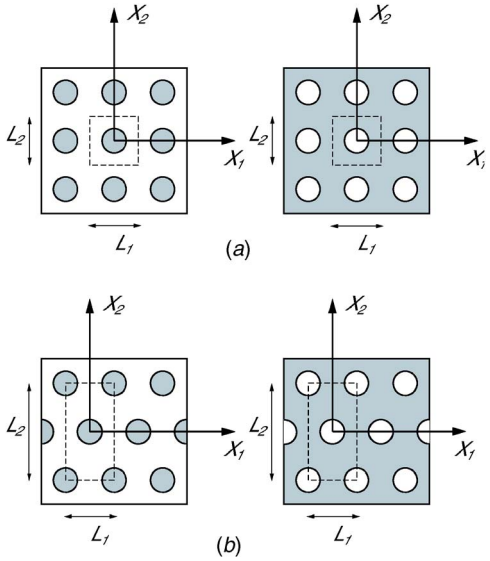

Fig. 2 Schematic representation of an infinite, perfectly periodic solid, with (*a*) square and (*b*) diagonal microgeometry

culated here are found by marching along (starting from $\lambda=0$) all radial paths $\varphi \in [0, 2\pi)$ in principal strain space for a fixed value of the "*principal axes orientation*" angle θ.

3.2 Constitutive Model. The theory presented thus far for the onset of failure in finitely strained periodic solids is valid for any rate-independent material with constitutive relations that can be put in the rate form (2.1). In the interest of (relative) simplicity, rubber-elastic materials are considered here because they have no memory of loading history and thus the final stress state of the unit cell depends only on the imposed final macroscopic strain. A compressible neo-Hookean constitutive law is adopted, which is a modified compressible 2D version of the standard *Mooney-Rivlin* solid, with strain energy density

$$W = \frac{\mu}{2}(I_1 - \ln I_2 - 2) + \frac{\kappa}{2}(\sqrt{I_2} - 1)^2, \tag{3.3}$$

in which μ is the solid's shear modulus at zero stress and κ determines its compressibility (for $\kappa/\mu \to \infty$ the solid becomes incompressible). Constants corresponding to the inclusion phase carry a subscript $_f$ (which stands for "*fiber*," since the microgeometry corresponds to a cross section of a fiber-reinforced solid) and constants corresponding to the matrix phase carry a subscript $_m$ (stands for "*matrix*"). Moreover, I_1 and I_2 are the two invariants of the right Cauchy-Green tensor $\mathbf{C}$,

$$I_1 = \mathrm{tr}\,\mathbf{C}, \quad I_2 = \det \mathbf{C}, \quad C_{ij} = F_{ki}F_{kj}, \tag{3.4}$$

and where $\mathbf{F}(\mathbf{X})$ is the deformation gradient tensor introduced in Sec. 2. Hence the components of the incremental moduli tensor $\mathbf{L}$, which enter the calculations for the onset of failure, are given by

$$L_{ijkl} = \frac{\partial^2 W}{\partial F_{ij} \partial F_{kl}}. \tag{3.5}$$

The reason for choosing this particular material lies in the fact that its strain energy density given by (3.3) is polyconvex in the sense of Ball [10], which guarantees the solid's rank one convexity at any deformation. This property precludes the appearance of strain discontinuities within each phase of the deformed unit cell.

3.3 F.E.M. Discretization and Condensation Algorithm. The unit cell of each periodic solid under consideration is discretized into standard two-dimensional quadrilateral isoparametric elements with bilinear shape functions, resulting in a four-node element with two degrees of freedom (d.o.f.) (one per each displacement component) per node. The unit cell of the periodic solid with the square microstructure (see Fig. 2(*a*)) is analyzed using an $N \times N$ rectangular (in parameter coordinate space) grid, while for the unit cell of the periodic solid with the diagonal microstructure (see Fig. 2(*b*)) an $N \times 2N$ rectangular (again in parameter coordinate space) grid is employed. To facilitate the application of periodicity requirements, both for the determination of the principal solution and for the Bloch wave-based stability investigations, corresponding nodes on opposite sides have the same coordinates in the reference configuration. Thus, corresponding nodes on sides AD (nodes with $X_1 = -L_1$ and denoted by $\mathbf{V}_l$) and BC (nodes with $X_1 = +L_1$ and denoted by $\mathbf{V}_r$) have the same X_2 coordinates and corresponding nodes on sides AB (nodes with $X_2 = -L_2$ and denoted by $\mathbf{V}_d$) and DC (nodes with $X_2 = +L_2$ and denoted by $\mathbf{V}_u$) have the same X_1 coordinates (see Fig. 3).

The principal solution for a given load path is calculated using a standard incremental Newton-Raphson technique, with a typical step size $\Delta\lambda = 10^{-3}$. This choice usually results in three iterations per step when an accuracy of 10^{-6} (based on a Euclidean displacement norm) is taken as the convergence criterion in each increment. For the case of orthotropic loading ($\theta=0$) only one-quarter of the unit cell is needed for the calculations. Due to symmetry, straightforward displacement conditions are applied on the boundaries of the positive quadrant. When the principal axes of strain are oriented at an angle with respect to the axes of orthotropy

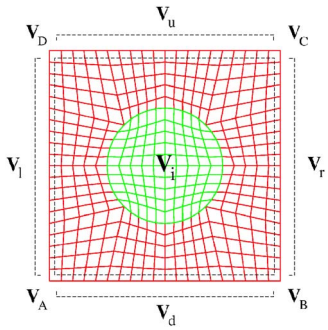

Fig. 3 Partition of the nodes of the discretized unit cell into internal and boundary ones, as required by the f.e.m.-based condensation technique employed in Bloch wave calculations

($\theta \neq 0$), the entire unit cell is used to calculate the principal solution by imposing appropriate coupling conditions to the nodes of opposite faces.

The stability analysis of the infinite periodic structure requires the consideration of all possible wave numbers $(\omega_1 L_1, \omega_2 L_2) \in \{[0, \pi) \times [0, \pi)\}$ for each equilibrium state along each loading path. A straightforward application of the Bloch wave theorem to find the minimum eigenvalue of the stability functional defined over the unit cell would require the numerical calculation of the minimum eigenvalue of an approximately $2N^2 \times 2N^2$ size complex stiffness matrix for the square and $2N^2 \times 4N^2$ size complex stiffness matrix for the diagonal microgeometry, respectively. Since this task would have to be repeated for each pair of wave numbers $(\omega_1 L_1, \omega_2 L_2)$, the scanning of a reasonably fine grid in the interval $[0, \pi) \times [0, \pi)$ would be prohibitively time consuming. Hence the need for an appropriate algorithm to address this issue becomes urgent.

The algorithm used to reduce the size of the stiffness matrices required for the Bloch wave calculations is based on a condensation technique and results in the eigenvalue sign determination of considerably smaller complex stiffness matrices, approximately $4N \times 4N$ for the square and $6N \times 6N$ for the diagonal microgeometry cell. The condensation technique is based on the observation that only boundary nodes need to be coupled in Bloch wave calculations and works as follows.

Of interest here is the lowest value λ_c of the load parameter λ for which the quadratic stability functional $\mathcal{F}_D(\lambda, \mathbf{v})$ loses its positive definiteness, i.e., its minimum eigenvalue $\beta(\lambda_c) = 0$, while $\beta(\lambda) > 0$ for $0 \leq \lambda < \lambda_c$ along the path. Consequently, in the finite element discretization of the problem one seeks the lowest value of the load parameter for which the quadratic form $F_D(\lambda, \mathbf{V})$ (which corresponds to $\mathcal{F}_D$) has a zero eigenvalue, and where

$$F_D(\lambda, \mathbf{V}) \equiv (\bar{\mathbf{V}})^{\mathbf{T}} \mathbf{K}(\lambda) \mathbf{V}. \tag{3.6}$$

Here $\mathbf{K}(\lambda)$ is the full (real and uncondensed) stiffness matrix corresponding to the f.e.m. discretization of the unit cell, and $\mathbf{V}$ is the nodal displacement vector corresponding to the discretization of $\mathbf{v}$. Notice that the components of the nodal displacement vector are not independent, but must satisfy the conditions imposed by the Bloch wave theorem, according to (2.6). To facilitate the calculations, the nodal numbering of the mesh is chosen such that

$$\mathbf{V} = (\mathbf{V}_i, \mathbf{V}_b, \mathbf{V}_t); \quad \mathbf{V}_b \equiv (\mathbf{V}_l, \mathbf{V}_d, \mathbf{V}_A), \quad \mathbf{V}_t \equiv (\mathbf{V}_r, \mathbf{V}_u, \mathbf{V}_B, \mathbf{V}_C, \mathbf{V}_D), \tag{3.7}$$

in which, as shown in Fig. 3, $\mathbf{V}_i$ are the d.o.f. corresponding to the unit cell's internal nodes, $\mathbf{V}_l$ and $\mathbf{V}_r$ are the d.o.f. corresponding to the left and right face of the unit cell, $\mathbf{V}_d$ and $\mathbf{V}_u$ are the d.o.f. corresponding to the lower and upper face of the unit cell and $\mathbf{V}_A$, $\mathbf{V}_B$, $\mathbf{V}_C$ and $\mathbf{V}_D$ are the d.o.f. corresponding to the four corner nodes of the unit cell. The above partition of the nodal displace-

ment vector $\mathbf{V}$ into internal and boundary d.o.f. parts also implies the corresponding partition of the uncondensed, tangent stiffness matrix $\mathbf{K}(\lambda)$

$$\mathbf{K}(\lambda)=\begin{bmatrix}\mathbf{K}_{ii}(\lambda) & \mathbf{K}_{ib}(\lambda) & \mathbf{K}_{it}(\lambda)\\ \mathbf{K}_{bi}(\lambda) & \mathbf{K}_{bb}(\lambda) & \mathbf{K}_{bt}(\lambda)\\ \mathbf{K}_{ti}(\lambda) & \mathbf{K}_{tb}(\lambda) & \mathbf{K}_{tt}(\lambda)\end{bmatrix}. \tag{3.8}$$

From the Bloch wave representation theorem (2.6), given that the finite element discretization is chosen such that corresponding nodes on opposite faces of the unit cell have one coordinate with the same value, one has the following relations between the boundary node d.o.f. of $\mathbf{V}$:

$$\mathbf{V}_r=\exp(2i\omega_1L_1)\mathbf{V}_l,\quad \mathbf{V}_u=\exp(2i\omega_2L_2)\mathbf{V}_d,$$

$$\mathbf{V}_B=\exp(2i\omega_1L_1)\mathbf{V}_A,\quad \mathbf{V}_D=\exp(2i\omega_2L_2)\mathbf{V}_A,$$

$$\mathbf{V}_C=\exp(2i\omega_1L_1)\exp(2i\omega_2L_2)\mathbf{V}_A. \tag{3.9}$$

Thus, one can connect $\mathbf{V}_b$ to $\mathbf{V}_t$, defined in (3.7) through a complex matrix $\mathbf{A}(\omega_1,\omega_2)$ whose nonzero entries are $\exp(2i\omega_1L_1)$ and $\exp(2i\omega_2L_2)$,

$$\mathbf{V}_t=\mathbf{A}(\omega_1,\omega_2)\mathbf{V}_b, \tag{3.10}$$

At the loss of positive definiteness of the quadratic form F_D, by solving $\mathbf{KV}=\mathbf{0}$ and expressing $\mathbf{V}_t$ and $\mathbf{V}_i$ in terms of $\mathbf{V}_b$, one can show that F_D can be equivalently expressed as a quadratic form involving only $\mathbf{V}_b$, namely,

$$F_D(\lambda,\omega_1,\omega_2)=(\overline{\mathbf{V}}_b)^T\hat{\mathbf{K}}(\lambda,\omega_1,\omega_2)\mathbf{V}_b, \tag{3.11}$$

in which the complex (Hermitian) matrix $\hat{\mathbf{K}}(\lambda,\omega_1,\omega_2)$ is expressed in terms of $\mathbf{A}$ and the submatrices on the uncondensed tangent stiffness $\mathbf{K}(\lambda)$ by

$$\hat{\mathbf{K}}=\mathbf{K}_{bb}+(\bar{\mathbf{A}})^T\mathbf{K}_{tb}+\mathbf{K}_{bt}\mathbf{A}+(\bar{\mathbf{A}})^T\mathbf{K}_{tt}\mathbf{A}$$
$$-[(\bar{\mathbf{A}})^T\mathbf{K}_{ti}+\mathbf{K}_{bi}](\mathbf{K}_{ii})^{-1}(\mathbf{K}_{ib}+\mathbf{K}_{it}\mathbf{A}). \tag{3.12}$$

The Bloch wave stability analysis of the infinite periodic medium requires along each loading path (fixed φ and θ) finding the lowest value λ_c of the load parameter λ for which there exists a pair of wave numbers $(\omega_{1c},\omega_{2c})$ (not necessarily unique due to symmetry) such that the Hermitian matrix $\hat{\mathbf{K}}(\lambda_c,\omega_{1c},\omega_{2c})$ is positive semi-definite, i.e., its lowest eigenvalue is zero. Thus, the microbuckling algorithm proceeds as follows: after determining the principal solution for each load parameter λ, the signature of the matrix $\hat{\mathbf{K}}(\lambda,\omega_1,\omega_2)$ is evaluated by performing an *LDU* decomposition of $\hat{\mathbf{K}}$. Positive definiteness is lost when the lowest entry of the Cholesky diagonal matrix D vanishes. This procedure is performed for each λ on a fine grid (grid spacing is $\pi/36$ in each direction) in wave number space. To investigate the special case when $\omega_i=0$ (i.e., when the eigenmode has period $2L_i$) the additional constraint $\mathbf{V}_{Ai}=0$ is also imposed.

Notice that in the expression for $\hat{\mathbf{K}}$ in (3.12) the inverse of $\mathbf{K}_{ii}(\lambda)$ appears which depends only on λ, the current load state. Hence, the inversion of $\mathbf{K}_{ii}(\lambda)$ is done only once (based on an *LDU* decomposition that takes advantage of the banded nature of this matrix). Consequently the calculations of the signature of all $\hat{\mathbf{K}}(\lambda,\omega_1,\omega_2)$'s on the grid points of the Fourier space are much quicker due to the considerably reduced (compared to the full d.o.f. of the unit cell) dimensions of these Hermitian matrices.

4 Results

The results of the numerical calculations are presented in Figs. 4–9 depicting the onset-of-failure surfaces for periodic composites with soft and hard inclusions, in macroscopic strain space where the coordinate axes are the principal logarithmic strains. All calculations reported here correspond to dimensions $R=0.5L$ and hence to a volume fraction of $\pi/16$ (approximately 20%). The case of voids is approximated by soft inclusions ($\mu_f/\mu_m=0.02$) and the case of rigid inclusions is approximated by stiff inclusions ($\mu_f/\mu_m=50.0$). The advantage of this approach is that the same unit cell mesh is employed for all inclusion-to-matrix stiffness ratios.

It should be mentioned here that such a complicated numerical algorithm requires a set of nontrivial checks in order to have confidence in its output. To this end, the numerical code used here was tested against the analytical calculations of [6] for the fiber-

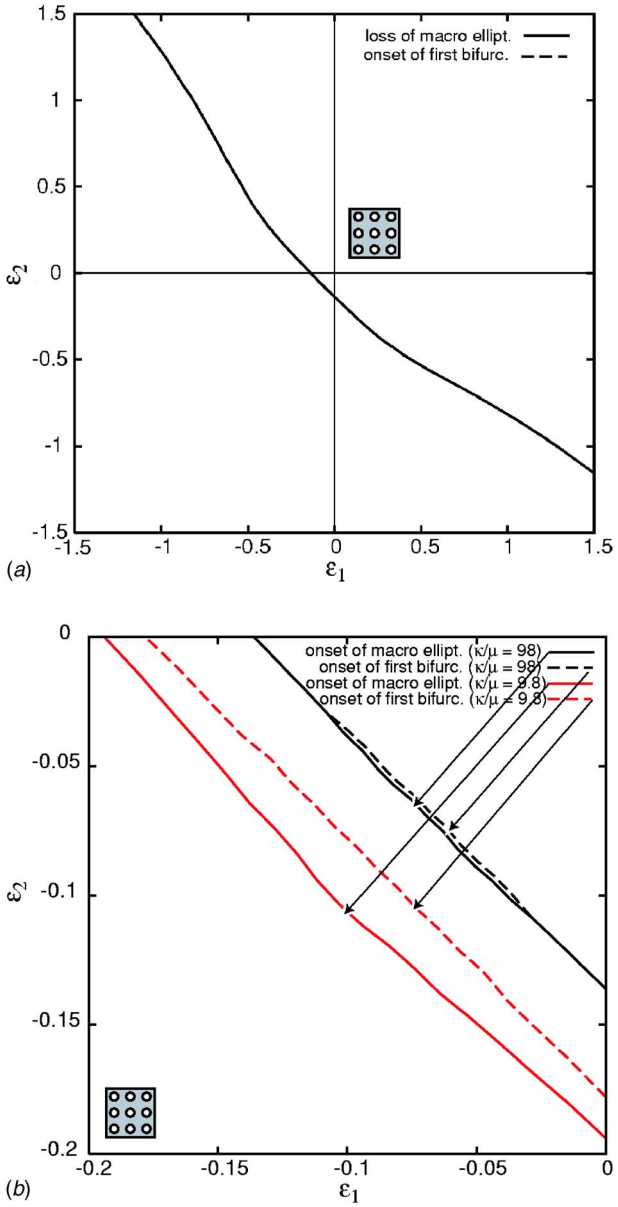

Fig. 4 In (*a*) are plotted the macroscopic (continuous line) and microscopic (dashed line) onset-of-failure surfaces in the principal macroscopic logarithmic strain space for a perfectly periodic, nearly incompressible ($\kappa/\mu=98$) solid, with a square distribution of voids ($\mu_f/\mu_m=0.02$) and subjected to biaxial loading along the initial axes of material orthotropy ($\theta=0$). In (*b*) is plotted a blow-up of the biaxial compression region showing that the first bifurcation occurs before the macroscopic loss of ellipticity. Note that the distance between the microscopic and macroscopic onset-of-failure surfaces increases with increasing compressibility of the material.

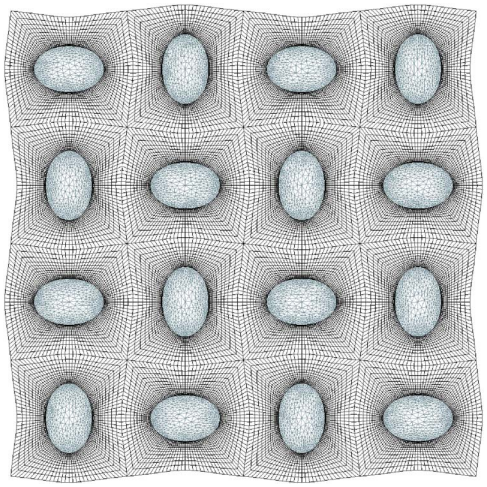

Fig. 5 Eigenmode of the microscopic bifurcation instability (antisymmetric in the unit cell) for balanced biaxial compression of the more compressible (κ/μ=9.8) voided solid examined in Fig. 4 (courtesy of Dr. J. C. Michel, CNRS-LMA, Marseille, France)

reinforced composite under combined compression and shear. By considering a rectangular unit cell of various aspect ratios made of two different layers, the Bloch wave and macroscopic loss of ellipticity predictions of the present code confirmed the results presented in the aforementioned paper. In addition, some of the loss of ellipticity calculations for the porous and the rigid inclusion case were repeated (based on a much finer unit cell f.e.m. mesh) by [11] providing an independent confirmation of the validity of our code. One should also point out the possibility of short wavelength interface instabilities at the matrix-inclusion boundary, which are inevitable at adequately large strains (see [12]). For the calculations reported here no such instabilities have been detected.

For the case of orthographically loaded (θ=0), nearly incompressible (κ/μ=98),[4] porous solids (μ_f/μ_m=0.02) with a square microgeometry, the macroscopic (solid line) and microscopic (dotted line) onset-of-failure surfaces are depicted in Fig. 4(*a*). As expected from the symmetry of the loading and of the microstructure, the graph is symmetric with respect to the diagonal $\epsilon_1=\epsilon_2$. Notice that for strains in the range $|\epsilon_i|\leqslant 1.5$ there is no instability under biaxial tension ($0\leqslant\varphi\leqslant\pi/2$) and that the most unstable region of the graph, i.e., the region with the lowest critical strains, is biaxial compression ($\pi\leqslant\varphi\leqslant 3\pi/2$). These results agree qualitatively with the loss of ellipticity numerical calculations of [13] (periodic, compressible Mooney-Rivlin-type solid) and the recent approximate analytical calculations of [14] (based on the same material and volume fraction but a random pore distribution).

Observe that at the scale used to plot the results in Fig. 4(*a*), the microscopic and macroscopic onset-of-failure surfaces appear to coincide. In reality the critical instability has a long wavelength (i.e., $\omega_c\rightarrow\mathbf{0}$) for most loading path angles φ, except within a region in the biaxial compression zone (about $\varphi=5\pi/4$) for which $(\omega_1 L_1)_c=(\omega_2 L_2)_c=\pi/2$. To better see the difference between the two onset-of-failure surfaces, Fig. 4(*b*) shows a magnification of the biaxial compression region in which one can clearly see the separation between the microscopic onset-of-failure surface (dotted line) and its macroscopic counterpart (solid line).

As it turns out, there is a strong dependence of the macroscopic and microscopic failure surfaces on the compressibility of the solid, which is depicted in Fig. 4(*b*). It is found that by increasing the compressibility tenfold (κ/μ=9.8), the onset of failure surfaces move further away from the origin and critical strains increase by approximately 40%. Moreover, there is a considerable increase in the separation between the microscopic and the macroscopic onset-of-failure surfaces for the more compressible material, although the critical wavelength of the microscopic buckling mode remains the same as in the nearly incompressible case. For the case of balanced biaxial loading in compression ($\varphi=5\pi/4$) of the solid with κ/μ=9.8, the eigenmode has been plotted at the onset of the first bifurcation instability, in Fig. 5 using a

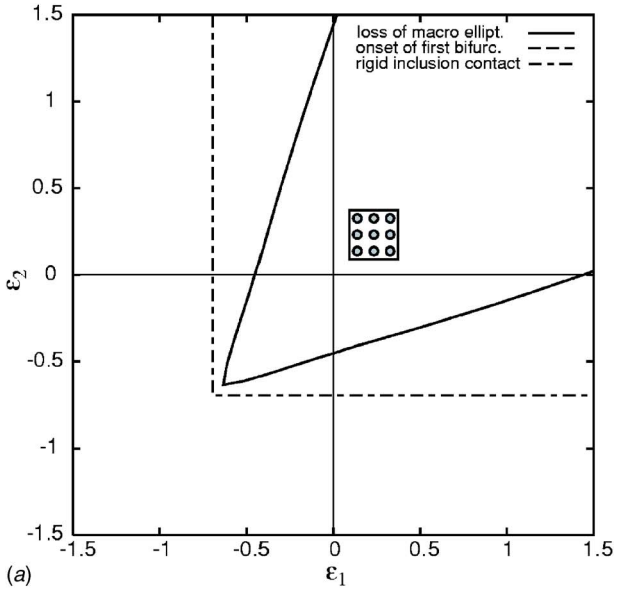

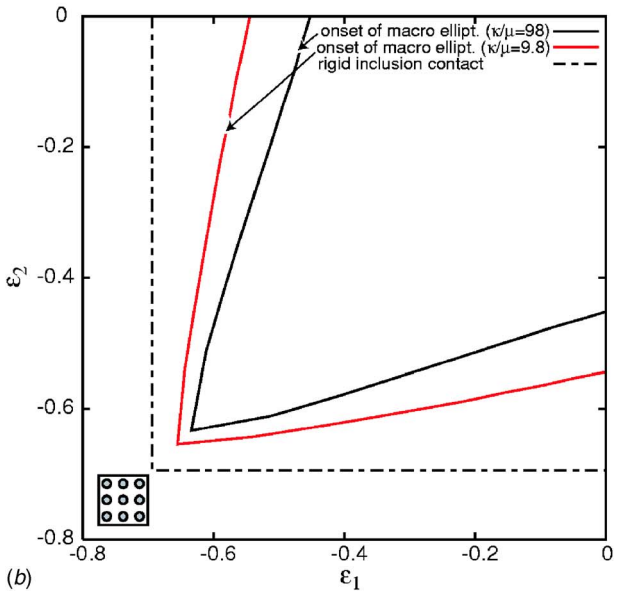

Fig. 6 In (*a*) are plotted the macroscopic and microscopic onset-of-failure surfaces in the principal macroscopic logarithmic strain space for a perfectly periodic, nearly incompressible (κ/μ=98) solid, with a square distribution of inclusions (μ_f/μ_m=50) and subjected to biaxial loading along the initial axes of material orthotropy (θ=0). Notice that the macroscopic and microscopic onset-of-failure surfaces coincide. The dotted-dashed line indicates macroscopic strains at which there is rigid inclusion contact. In (*b*) is plotted a blow-up of the biaxial compression region showing the influence of material compressibility.

[4]The absence of subscripts indicates that the compressibility ratio has the same value in each phase.

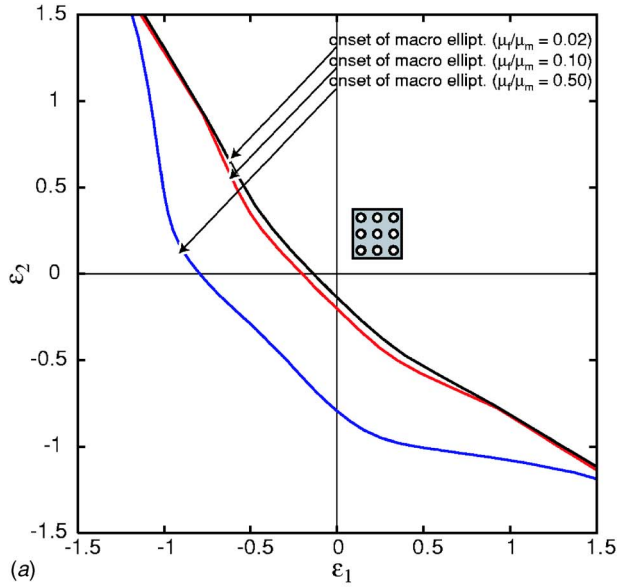

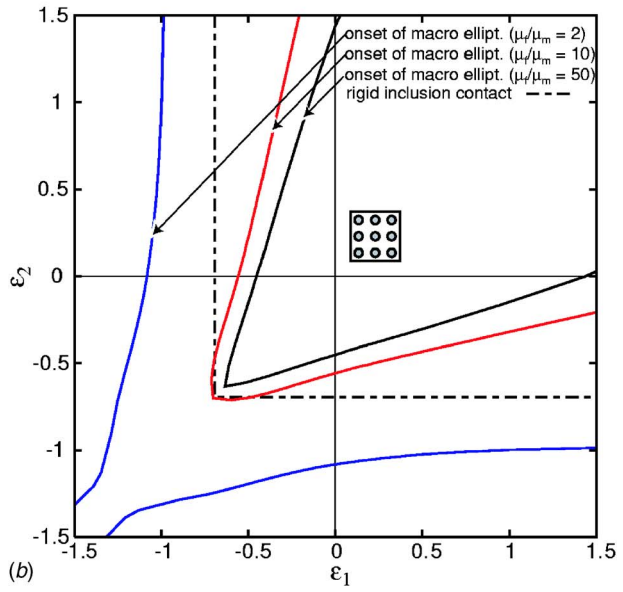

Fig. 7 Influence of changing the stiffness contrast on the onset-of-failure surfaces for (*a*) weaker than the matrix (μ_f/μ_m =0.02,0.1,0.5) and (*b*) stronger than the matrix (μ_f/μ_m =2.0,10.0,50.0) inclusions under orthotropic loading and for a square microgeometry arrangement

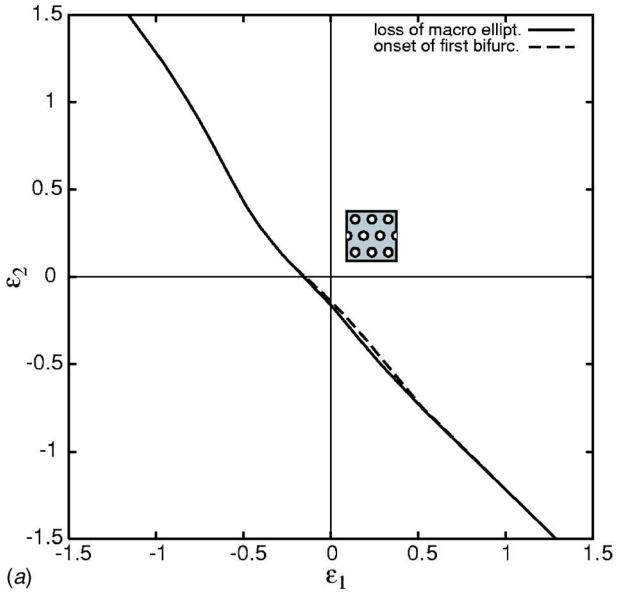

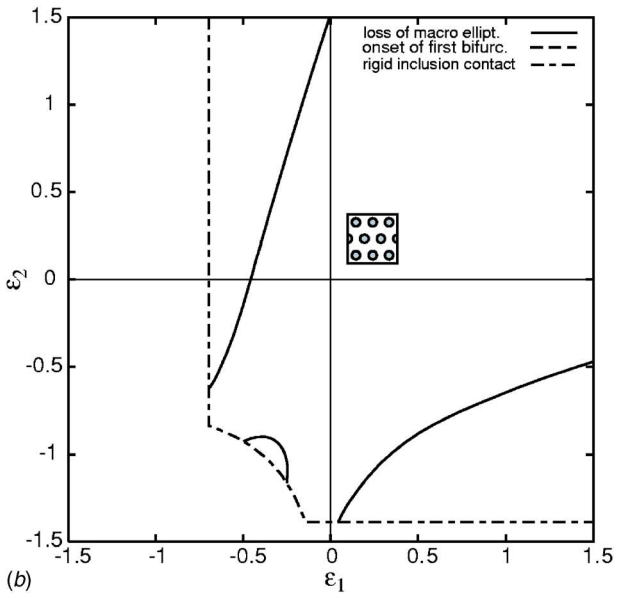

Fig. 8 Influence of changing the stiffness contrast on the onset-of-failure surfaces for (*a*) the voided solid (μ_f/μ_m=0.02) and (*b*) the solid with rigid inclusions (μ_f/μ_m=50.0) under orthotropic loading and for a diagonal microgeometry arrangement

4×4 cell region of the periodic solid. This picture clearly shows the antisymmetric bifurcation mode (the repeating unit pattern of the eigenmode is a 2×2 cell region).

The stability results for the case of orthotropically loaded (θ =0) solids with periodic rigid inclusions (μ_f/μ_m=50) with the same microgeometry and the same compressibility as in Fig. 4(*a*) are depicted in Fig. 6(*a*). The dotted-dashed line represents the locus of points in principal logarithmic strain space where there is inclusion contact (easily calculated from geometry, assuming perfectly rigid inclusions). Again all graphs are symmetric with respect to the diagonal $\varepsilon_1=\varepsilon_2$, as expected from the symmetry of the loading and of the underlying microstructure. The critical strains in biaxial compression are much higher (about five times) than in the case the corresponding porous solids. Also unlike the porous case, the microscopic and macroscopic onset-of-failure surfaces of the solid with rigid inclusions are always coincident, thus indicating that the critical mode at instability is a long wavelength one (i.e., $\boldsymbol{\omega}_c\rightarrow\mathbf{0}$) for all loading path angles. Also note that no instability is detected here in the biaxial tension region ($0\leqslant\varphi\leqslant\pi/2$) for $\varepsilon_i<1.5$.

As expected from the voided solid case, compressibility plays an important role on failure, and the comparison of the onset-of-failure surfaces for two different compressibilities (κ/μ=98 and κ/μ=9.8) is presented in Fig. 6(*b*). As for the voided case, an increase in compressibility in the solid with periodic inclusions leads to higher critical strains, although the increase of the critical strains is less dramatic than in the voided solid of the same volume fraction and microgeometry.

The influence of the stiffness contrast between the inclusion and matrix phases μ_f/μ_m on the stability of the nearly incompressible (κ/μ=98) periodic solid with a square microgeometry is depicted in Fig. 7. More specifically Fig. 7(*a*) shows the onset-of-failure

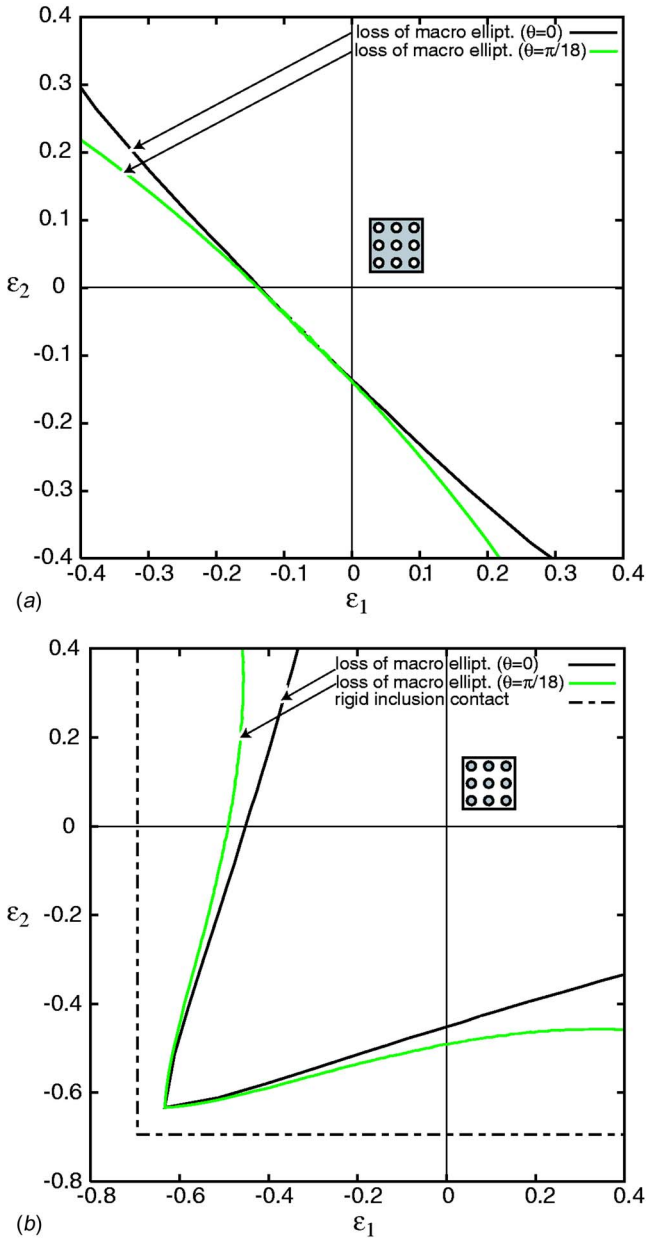

Fig. 9 Influence of principal axes orientation θ on the onset-of-failure surfaces for a perfectly periodic solid, with (*a*) a square distribution of voids ($\mu_f/\mu_m=0.02$) and (*b*) a square distribution of rigid inclusions ($\mu_f/\mu_m=50$). Observe the increase in the critical strains from a loading at a angle $\theta=0$ to a loading at angle $\theta=\pi/18$ with respect to the initial axes of material orthotropy.

surfaces for three stiffness ratios $\mu_f/\mu_m=0.02,0.1,0.5$ (lowest number corresponds to voided solid) while Fig. 7(*b*) shows the onset-of-failure surfaces for three stiffness ratios $\mu_f/\mu_m=2,10,50$ (highest number corresponds to solid with rigid inclusions). In both cases a decrease in the stiffness contrast between the two phases increases the strains at the onset of failure as expected from continuity since for $\mu_f/\mu_m=1$ the solid is uniform and strongly elliptic at all strains. Again the graphs are symmetric with respect to the diagonal $\varepsilon_1=\varepsilon_2$ and the microscopic and macroscopic onset-of-failure surfaces coincide in all cases except for the voided solid ($\mu_f/\mu_m=0.02$) near balanced biaxial compression ($\varphi=5\pi/4$), a difference which is not discernible at the scale for which the results are plotted. It is also worth mentioning the highly nonlinear dependence of the results on the stiffness contrast, since the first fivefold change in the voided (from $\mu_f/\mu_m=0.02$ to 0.1) or in the rigid inclusion (from $\mu_f/\mu_m=50$ to 10) case produces considerably smaller changes in the onset-of-failure surface than the next fivefold change in the same stiffness contrast.

The importance of the microgeometry on the onset-of-failure surfaces is shown in Fig. 8(*a*) and 8(*b*) which correspond to the voided and rigid inclusion cases, respectively, but with a diagonal microgeometric arrangement of the inclusions (volume fraction is kept constant). The onset-of-failure surfaces for the voided diagonal microgeometry case in Fig. 8(*a*) does not look much different from its square microgeometry counterpart in Fig. 4(*a*), save for the nonsymmetry of the graphs with respect to the diagonal $\epsilon_1=\epsilon_2$ and the fact that there is a much broader range of the loading path angle φ for which a microbuckling instability precedes the microscopic loss of ellipticity. The microgeometry influence is considerably more dramatic for the rigid inclusion case, as a comparison between Figs. 6(*b*) and 8(*b*) shows (the dotted-dashed line again corresponds to fiber contact). Observe that in the diagonal inclusion arrangement there are loading paths in biaxial compression for which the material shows no microscopic instability (and remains macroscopically elliptic) until inclusion contact. Also note the large difference in the stability properties along the two different axes of orthotropy.

Finally the influence of principal strain axes orientation θ with respect to the axes of orthotropy is presented in Fig. 9, which compares the onset-of-failure surfaces of the two-phase periodic solids with diagonal microgeometry for loading along the axes of orthotropy ($\theta=0$) and for loading at a fixed angle with respect to the axes of orthotropy ($\theta=\pi/18$). The comparison for the voided case ($\mu_f/\mu_m=0.02$) is presented in Fig. 9(*a*), which shows no appreciable influence of the principal strain axes orientation on the onset-of-failure surfaces in the biaxial compression region, but shows substantial stabilization for the nonorthotropic loading case (i.e., higher critical strains) in the remaining regions where one strain is tensile. As in the orthotropic loading case, for the nonorthotropic loading there is also a difference between the macroscopic and macroscopic onset-of-failure surfaces in the biaxial compression region (for both principal strain axes orientations the eigenmode is local in nature; it is antisymmetric on the unit cell with $(\omega_1 L_1)_c=(\omega_2 L_2)_c=\pi/2$). However, due to the scale of the graph, the corresponding curves appear to coincide.

The comparison for the rigid inclusion case ($\mu_f/\mu_m=50.0$) is presented in Fig. 9(*b*), which shows a significant and increasing stabilization for the nonorthotropically loaded solid (i.e., higher critical strains) as the loading path angle moves away from the balanced biaxial compression ($\varphi=5\pi/4$). Similar to the orthotropic loading case, for the nonorthotropic loading the microscopic and macroscopic onset-of-failure surfaces are found to coincide. It is noteworthy that a small deviation ($\theta=\pi/18$) of the principal strain axes from the axes of orthotropy produces significant increases in the failure strains for both the voided and the rigid inclusion case. The finding for the voided case is consistent with results for aluminum honeycomb (see [5]) for which nonorthotropic loading leads to an expansion of the onset-of-failure surface, i.e., to higher critical stresses.

The above results show the strong influence of compressibility (κ/μ) and of principal axes orientation (θ) on the onset-of-failure surfaces for voided as well as solids with rigid inclusions. The solid's microgeometry has a much more important influence on the onset-of-failure surfaces for the case of rigid inclusions. Note that the above results pertain to perfect solids, thus raising the very important question of the influence of imperfections, which is the subject of a subsequent investigation.

5 Discussion and Conclusions

The[5] above-presented work connects the onset of a microscopic (bifurcation-type) instability to its corresponding macroscopic (loss of ellipticity in the homogenized tangent moduli) counterpart in periodic continua of infinite extent, thus ignoring boundary effects (for continua, the loss of ellipticity signals an instability under Dirichlet boundary conditions). Finding the microscopic instability of a periodic solid of infinite extent that has a continuum unit cell requires a novel numerical (f.e.m.-based) technique, introduced in this paper to expedite the corresponding Bloch wave calculations. The solids considered here are two-phase hyperelastic, compressible neo-Hookean solids that satisfy in each phase the strong ellipticity condition for arbitrary strains. Periodically spaced circular inclusions are considered in two different microgeometric arrangements (one square and one diagonal), both having the same volume fraction. By varying the inclusion-to-matrix stiffness ratio one can investigate the stability of a wide variety of periodic continua, from porous solids all the way to solids with rigid inclusions. The stability results are presented in macroscopic logarithmic strain space for arbitrary plane strain loading and show both the microscopic instability (onset of the first bifurcation in the infinite, perfect periodic composite) and the corresponding macroscopic instability (onset of the loss of ellipticity in the homogenized tangent moduli of the initial unit cell).

For porous solids loaded so that the principal strains are aligned with the axes of orthotropy, the most unstable region is biaxial compression. Although the matrix constitutive law and the volume fraction are not the same, the shape of the loss of ellipticity curves is in agreement with earlier results of [13]. However, in the biaxial compression region of principal strain space, the macroscopic loss of ellipticity is preceded by a microscopic instability with a local bifurcation eigenmode (antisymmetric in each direction of the unit cell). The distance between the corresponding micro and macro onset-of-failure surfaces is found to increase significantly with a modest increase in the solid's compressibility. At the same time both microscopic and macroscopic onset-of-failure surfaces expand with compressibility, thus showing considerable overall stabilization of the more compressible solid under biaxial compression. It has also been found that even a small deviation of the principal axes of strain from the axes of orthotropy of the composite results in a significant change of the failure surfaces.

At the same time, the change in microgeometry does not result in any important change of the failure surfaces for the porous solids, particularly under conditions of biaxial compression, assuming that the volume fraction remains constant. This result is in agreement with recent calculations on the same solid by [14] who find that solids of the same volume fraction, but a random distribution of equidisperse pores have the same qualitative response for the loss of ellipticity of their homogenized solid. The explanation to this phenomenon has to be found in the response of imperfect solids, which show a loss of stability at strains close to the bifurcation strains of the perfect structure (bifurcation points of the perfect composite become limit loads for its imperfect counterpart). Preliminary calculations by [11] support this assertion.

The case of solids reinforced with rigid inclusions has several major differences from the periodic porous solids with the same matrix material and microgeometry. First, the microscopic and macroscopic onset-of-failure surfaces are always coincident, thus indicating that the long wavelength eigenmode is the critical one for all possible loading paths. Moreover, the composite is considerably more stable under balanced biaxial compressive strains than under uniaxial compressive strains and the corresponding onset-of-failure strains are an order of magnitude larger than their counterparts for porous solids with the same matrix material and microgeometry. The distance between the corresponding microscopic and macroscopic onset-of-failure surfaces is found to increase significantly with a small increase in the solid's compressibility and the failure surfaces expand, thus showing considerable overall stabilization of the more compressible solid. Similar to the case of porous solids, even a small deviation of the principal axes of strain from the axes of orthotropy of the composite results in significant change of the failure surfaces.

In contrast to the porous solid case, changes in microgeometry have significant influence on the onset-of-failure surfaces for solids with rigid inclusions. For this case, the comparison of the loss of ellipticity for the periodic and random composite with the same volume fraction of inclusions is not possible, since calculations for the same matrix material with an equidisperse case of randomly distributed rigid inclusions shows no loss of ellipticity in the resulting composite. Again the explanation has to be found in the influence of imperfections. Preliminary calculations by [11] in composites with inclusions show that a slight perturbation in the periodicity of the microgeometry results in a dramatic expansion of the onset-of-failure surface, thus explaining why solids with the same matrix material, but randomly reinforced with rigid inclusions, remain elliptic.

The connection between the stability of composites with randomly distributed and periodically arranged inclusions requires understanding of the imperfection sensitivity of these structures. To this end it is important to investigate the post-bifurcated solutions emerging at critical points. For porous composites, preliminary calculations of imperfect many-cell assemblies indicate that the bifurcated solutions are unstable [11], while the opposite occurs for the case of inclusions. In addition to post-bifurcated equilibria and imperfection sensitivity, there are important remaining questions about the influence of volume fraction, microgeometry, and constitutive behavior of the nonlinear matrix material. These issues are currently the object of intense investigations which hopefully will soon bear fruit.

[5]We are grateful to the authors of [15] who confirmed that the macroscopic moduli of their randomly, particle-reinforced material are strongly elliptic.

Acknowledgment

This work was supported by AFOSR under Grant No. F49620-99-1-0098 to the University of Michigan. The authors would like to acknowledge many helpful discussions with Dr. J. C. Michel of the CNRS Laboratory in Mechanics and Acoustics at Marseille, France, who also provided the calculations depicted in Fig. 5 and Prof. P. Ponte-Castañeda of the Ecole Polytechnique in Paris for many discussions on the stability properties of composites with random microstructures.

References

[1] Triantafyllidis, N., and Maker, B. N., 1985, "On the Comparison Between Microscopic and Macroscopic Instability Mechanisms in a Class of Fiber-Reinforced Composites," ASME J. Appl. Mech., **52**, pp. 794–800.

[2] Geymonat, G., Müller, S., and Triantafyllidis, N., 1993, "Homogenization of Nonlinearly Elastic Materials, Microscopic Bifurcation and Macroscopic Loss of Rank-One Convexity," Arch. Ration. Mech. Anal., **122**, pp. 231–290.

[3] Triantafyllidis, N., and Bardenhagen, S. G., 1996, "The Influence of Scale Size on the Stability of Periodic Solids and the Role of Associated Higher Order Gradient Continuum Models," J. Mech. Phys. Solids, **44**, pp. 1891–1928.

[4] Schraad, M. W., and Triantafyllidis, N., 1997, "Scale Effects in Media With Periodic and Nearly Periodic Microstructures, II—Failure Mechanisms," ASME J. Appl. Mech., **64**, pp. 763–771.

[5] Triantafyllidis, N., and Bardenhagen, S. G., 1996, "Onset of Failure in Aluminum Honeycombs Under General In-plane Loading," J. Mech. Phys. Solids, **46**, pp. 1089–1124.

[6] Nestorović, M., and Triantafyllidis, N., 2004, "Onset of Failure in Finitely Strained Layered Composites Subjected to Combined Normal and Shear Loading," J. Mech. Phys. Solids, **52**, pp. 941–974.

[7] Gong, L., Kyriakides, S., and Triantafyllidis, N., 2005, "On the Stability of

Kelvin Cell Foams Under Compressive Loads," J. Mech. Phys. Solids, **53**, pp. 771–794.
[8] Hill, R., 1958, "A General Theory of Uniqueness and Stability in Elastic-Plastic Solids," J. Mech. Phys. Solids, **6**, pp. 236–249.
[9] Nguyen, Q. S., and Triantafyllidis, N., 1989, "Plastic Bifurcation and Postbifurcation Analysis for Generalized Standard Continua," J. Mech. Phys. Solids, **37**, pp. 545–566.
[10] Ball, J. M., 1977, "Convexity Conditions and Existence Theorems in Nonlinear Elasticity," Arch. Ration. Mech. Anal., **63**, pp. 337–403.
[11] Michel, J. C., 2005, work in preparation for publication.
[12] Biot, M. A., 1965, *Mechanics of Incremental Deformation*, Wiley, New York.
[13] Abeyaratne, R., and Triantafyllidis, N., 1984, "An Investigation of Localization in a Porous Elastic Material Using Homogenization Theory," ASME J. Appl. Mech., **51**, pp. 481–486.
[14] Lopez-Pamiez, O., and Ponte-Castañeda, P., 2004, "Second-Order Estimates for the Macroscopic Response and Loss of Ellipticity in Porous Rubbers at Large Deformations," J. Exp. Zool., **76**, pp. 247–287.
[15] Lopez-Pamiez, O., and Ponte-Castañeda, P., 2003, "Second-Order Estimates for the Macroscopic for the Large Deformation Response of Particle Reinforced Rubbers," C. R. Mec., **331**, pp. 1–8.